Journal of Modern Optics

Vol. 00, No. 00, DD Month 200x, 1–10

Wavefront curvature sensing for the human eye

Cristiano Torti*, Steve Gruppetta and Luis Diaz-Santana†

Applied Vision Research Centre, The Henry Wellcome Laboratories for Vision Science, City University,

Northampton Square, London, EC1V 0HB UK

(Received 00 Month 200x; in final form 00 Month 200x)

In this paper we present a curvature wavefront sensor for the eye. The layout proposed is novel, whilst the algorithm used has been adapted from previously published work [1]. The design of the set-up incorporates two field lenses that, together with a beam separator, define the distance Δz between the two defocused planes. We present a feasibility study to use this particular combination of optical configuration and retrieval algorithm in the eye. We present calibration curves and results from three real eyes.

1 Introduction

Over the last ten years there has been an increased interest in the measurement and understanding of the aberrations of the human eye [2–4]. A number of techniques for this purpose have been proposed, the most common being the Shack-Hartmann (SH) sensor based on the implementation by Liang *et al.* [5]. Currently, a number of commercial SH sensors for the eye are available. However, the constant pressure for improved performance [6], like extending the sensor's dynamic range [7], sensitivity [8], speed [9], robustness to scattering and opacities has lead to the development of other wavefront sensing techniques for the eye. Amongst them, and currently available either in research laboratories, commercial instruments or both we find laser ray tracing (RT) [7], pyramid wave front sensing [8], curvature sensing [10], and a sensor based on the Talbot Effect [11]. Very recently a new holographic wave front sensor for the eye has also been proposed, although experimental verification is pending [12]. Curvature sensors (CS) have

*Currently at Cardiff University , UK

†Corresponding author. Email: L.Diaz-Santana@city.ac.uk

Journal of Modern Optics

ISSN 0950-0340 print/ISSN 1362-3044 online

http://www.tandf.co.uk/journals

DOI: 10.1080/0950034YYxxxxxxxx

historically been applied to non-ophthalmic applications. However, in 2005 a CS was developed to measure the topography of the human cornea [13, 14]. And only last year, a CS was developed to measure ocular aberrations with a performance comparable to a SH sensor [10].

Curvature sensors may present distinct advantages for ocular wavefront sensing over other techniques. Due to the differential nature of the CS's signal, it is expected it to be less affected by ocular scattering and speckle noise [15]. Also, unlike the SH sensor, whose sampling is limited by the number and pitch of the lenslet sub-apertures, one might exploit high resolution imaging detectors (eg. CCDs) to achieve a sampling that is only limited by the resolution of the detector itself.

In this paper we describe an alternative implementation of a CS not previously applied to the eye, together with a reconstruction algorithm [1] similar to that in reference [16], but using two defocused images instead of only one. The aim of this paper is to describe this implementation, show calibration data and to show that the quality of the signal permits our algorithm to reconstruct wavefronts that are in line with expectations when comparing them with the subjects' known prescriptions. Our current purpose does not stretch out to explore the limitations on the technique imposed by the boundary conditions, scattering or speckle present on the sensor. More information on some of these topics can be found in references [15, 17]. Future work will address these issues in more detail. This work must be regarded as a feasibility study, not as a full characterisation of the sensor.

In curvature sensing two measurements of the intensity distribution of a beam along the direction of propagation are recorded. Reference [18] and references within show that the normalized difference between those two intensities is proportional to the Laplacian (*i.e.* curvature) of the wavefront within the pupil, and to the normal derivative of the wavefront along the pupil boundary. The curvature signal S is defined as the point-to-point contrast between the two recorded intensities:

$$S \equiv \frac{I_1 - I_2}{I_1 + I_2} = \left(\frac{\partial W}{\partial n}\, \delta_c - \mathcal{P}\, \nabla^2 W \right) \Delta z \tag{1}$$

where $I_1(x, y, \Delta z)$ and $I_2(x, y, -\Delta z)$ are the intensity distributions in planes $P_1(x, y, \Delta z)$ and

$P_2(x, y, -\Delta z)$, respectively, Δz is the distance between planes $P_1(x, y, \Delta z)$ and $P_2(x, y, -\Delta z)$, $W(x, y, 0)$ is the wavefront distribution at $P(x, y, 0)$, $\partial/\partial\mathbf{n}$ is the normal derivative operator, $\nabla^2 \equiv (\partial^2/\partial x^2 + \partial^2/\partial y^2)$ is the Laplacian operator, $\mathcal{P}$ is the pupil transmittance function (1 inside the pupil and 0 outside), and δ_c is a circular Dirac delta distribution at the pupil boundary. The arguments were omitted from Eq. 1 for clarity.

2 Optical Set-up

The design proposed for curvature sensing allows two symmetrically defocused pupil images to be taken simultaneously, without the need to either switch between two different physical planes or to synchronise and calibrate two cameras. The optical set-up is depicted in Fig. 1. An objective (O) and pinhole (PH) are used to spatially filter a 670 nm laser diode (LD) beam. The beam is collimated by an achromatic lens (CL_1) ($f_{CL_1} = 100$ mm) and a diaphragm (D_1) is used to reduce the beam diameter to 1 mm to be delivered into the subject's eye. The subject's head is placed against a headrest that helps to keep the subject's pupil coincident with the pupil plane of the optical system. We did not use a bite bar. The axis of the beam which enters the eye is slightly displaced from the axis of the CS to help send corneal reflections off-axis. If corneal refections still persist, the subject is asked to tilt his/her line-of-sight slightly off-axis with respect to the beam and/or translate their head slightly so that the beam is off-axis to that of the eye. The power reaching the eye was 200nm in power.The beam that follows into the CS branch is focused by an achromatic lens (L) ($f_L = 200$ mm) into two foci via a beam-splitting beam-separator (BSS), which provides a lateral beam displacement of 20 mm. Matching positive and negative field lenses (FL) ($f_{FL} = \pm$ 500 mm) are placed in the focal planes of lens L. The beams are re-collimated by identical achromatic lenses (CL_2) ($f_{CL_2} = 200$ mm) and demagnified using a telescope consisting of achromatic lenses TL_1 ($f_{TL_1} = 200$ mm) and TL_2 ($f_{TL_2} = 40$ mm) allowing both beams to be imaged by a single CCD camera (CCD) Rolera-XR (from Qimaging). A second diaphragm (D_2) is used to further help eliminate corneal reflections.

The relative path length difference introduced by the BSS together with the opposing powers of the

FLs result in a physical separation between the two pupil conjugates P'. When the camera is positioned conjugate to the plane halfway between the two conjugates P', two symmetrically defocused pupil images are obtained. The planes P_1' and P_2', corresponding to the two defocused images I_1 and I_2 are conjugates of a plane behind (P_1) and in front (P_2) of the pupil of the eye P. By changing the power of FL the sensor's sensitivity can be tuned by effectively varying the amount of separation between P_1 and P_2 ($2\Delta z$ in Eq. 1). Thus, this design permits to change the sensors' sensitivity without altering the magnification of the beam in the sensing plane. In this case one does not need to be concerned with the change of pixel sampling as the sensitivity is changed. Nor is there a risk of the beam size increasing beyond the physical size of the detector.

Starting with the beam displacement introduced by the beam separator, it is easy to show that the separation between the object planes relative to the pupil plane (Δz) can be increased or decreased by varying the powers of the field lenses and/or by reversing their positions. The plane separation Δz is related to the focal length of CL_2 and the focal length of the field lenses ($\pm f_{FL}$) by

$$\Delta z = \frac{f^2}{|f_{FL}|} + \frac{d_{BS}}{2} \tag{2}$$

where f is the focal length of CL_2, and d_{BS} is the axial displacement of the two beams due to the beam separator.

In fact, realistic values for the focal lengths of the field lenses restrict the achievable plane separations. In effect, a range of 34 mm to 4 km is achievable with the use of field lenses ranging from 1000 mm to 10 mm with 200 mm focal lengths for CL_2 and 12 mm separation introduced by BSS. Although, in practise, beams with several diopters of vergence may be vignetted imposing further constrains to the actual dynamic range of a particular system. This will depend on the particular design of the system, including lens apertures and size of the CCD detector. Care must be taken when designing such a system that these constrains are understood and vignetting does not occur. In the absence of vingetting the dynamic range of the system will be set by Δz alone [19].

For the current system parameters $\Delta z = 86$mm in accordance with Eq. 2. This value was later experimentally fine tuned as described in Section 4. The system response was experimentally validated to ensure vignetting did not occur over the range -4D to +3D of defocus and -4.5D to +5.5D of astigmatism. Calibration data is presented below in Section 4. This same value of Δz was used for all the subjects measured in this study and the calibration of the set-up.

3 Wavefront retrieval

Each pixel on the CCD sampled approximately 68μm over the pupil plane. Wavefront reconstruction was obtained using a Gerchberg-type algorithm (GA) – an iterative, discrete Fourier transform domain filtering technique [1]. The GA exploits the fact that a Laplacian in object space is proportional to a multiplication by the angular frequency squared $(u^2 + v^2)$ in Fourier space. The Laplacian operator can be expressed, in Fourier space, by

$$\left(\frac{\partial^2}{\partial x^2} + \frac{\partial^2}{\partial y^2}\right) \overset{\mathcal{F}}{\underset{\mathcal{F}^{-1}}{\rightleftharpoons}} (-i\,2\,\pi)^2\,(u^2 + v^2) \tag{3}$$

where u and v are the spatial frequencies, $\mathcal{F}$ and $\mathcal{F}^{-1}$ are the Fourier transform pair operators and i is $\sqrt{-}1$. Thus, it is simple to invert the Laplacian operator in Fourier space to solve for W in Eq. 1. However, since S is bounded, the simple relationship described above no longer holds, and so S must be extrapolated. This is achieved by imposing Neumann boundary conditions along the boundary.

The reconstruction algorithm is illustrated in Fig. 2. In the first part (right side), the above mentioned Fourier technique is applied to the sensor signal S to estimate W. In the second part (left side), the boundary conditions are applied to the normal derivative of W. For this, the radial derivative of W is set to zero along a narrow band around the sensor signal boundary. The band is created by subtracting the binary masks obtained by dilating and eroding an estimated binary mask for the sensor signal by one pixel. The total thickness of the band is thus two pixels although its precise thickness was not found to

be crucial. The Laplacian of the estimated wavefront is replaced with the experimental data within the region bounded by the narrow band whilst keeping the extrapolated signal on and outside of the band.

The root-mean-squared (RMS) difference between the wavefront estimates from one iteration to the next is used as a stopping criterion. The final wavefront estimate is taken to be the portion within the estimated pupil boundary. This boundary is estimated by creating a binary mask whose radius is equal to the mean radius of the two out-of-focus images. The convergence follows a base 10 logarithmic decline with iteration. Wavefront reconstructions can be obtained in three seconds using Matlab (including both the image extraction and the GA with four iterations), achieving a wavefront RMS difference of less than 5%.

4 Calibration

The sensor was calibrated using trial lenses of known sphere. The resulting sensor response curve over the range -4 to +3 diopters is shown in Fig. 3(a). Note that this is the range known to be free of vignetting as discussed in Section 2. The response is highly linear over most of the range. Also shown is a plot of the residuals, where the residuals are defined as the absolute difference between the measured sphere and the expected value according to the slope of the linear fit. The residuals plot helps us to define the region over which the sensor's response is linear to defocus, and hence its dynamic range. The linear fit was accordingly repeated over this region (-3 to +2.5D). The resulting slope was used as a calibration factor multiplying the nominal value of Δz obtained from Eq. 2 for all subsequent analysis. Note that the error in the estimation of defocus seems to be larger near zero than in the rest of the region of linear response. The origin of this error was not characterised and will be addressed in the future.

Using this calibration factor, the sensor's response to cylindrical trial lenses was verified. The resulting response curves for cylindrical trial lenses at approximately 0° and 45° is shown in Fig. 3(b) and Fig. 3(c) respectively. Once again, the response curves are highly linear over a range of several diopters. The linearity was within 10% for the data taken at approximately 0° over the range -4.5 to +5.5 diopters, and within 7% for the data taken at approximately 45° over the range -4.5 to +3 diopters. Based on the relative

slopes of the curves for 0°, the cylindrical lenses were oriented with their axes at approximately 3.0° with respect to the CCD array. Similarly, for the data set taken at nearly 45°, the true approximate angle was found to be 43.8°.

5 Results

After calibration, the system was further tested using a phase plate encoding the aberrations of a real eye [20]. A number of interferograms of the phase plate from a Mach-Zender interferometer (MZI) were recorded for comparison. One of these interferograms is shown in Fig. 4(a). The phase plate did not encode any defocus, whilst the estimated wavefronts yielded -0.4 μm (-0.3 D) of defocus. This overestimation of defocus may be a consequence of the larger error for defocus towards the origin of the calibration plot (Fig. 3(a)) mentioned in section 4 together with a small amount of residual defocus in the system. The simulated interferogram obtained from the retrieved wavefront shown in Fig. 4(b) is that obtained after removing defocus from the wavefront. Future work will address the origin of this error in further detail.

The aberrations from three eyes from three young adults were measured using the system. None of them presented any previous known ocular pathology, and all of them have low prescriptions. Their prescriptions were as follows Subject 1 +0.25DS, Subject 2 +0.5/-1.25×170 and Subject 3 plano/plano. Two examples of raw signal data are shown in Fig. 5. Subject 1 had a significantly larger pupil than subject 2 hence the larger circles in the top panel.

Figure 6 shows the results obtained from these 3 eyes. All results shown are an average of 18 measurements. The left column shows the wavefront estimated from the curvature sensor using the algorithm described in Section 3. The right hand side column shows the magnitude of the Zernike coefficients obtained from a least square fit to the wavefront on the left using a Zernike polynomial base. The ordering of the polynomials used was that of Noll [21]. The subjects' prescriptions estimated from these data are as follows: Subject 1 presented -0.67/-0.26×51 with standard deviations of 0.10/0.15×18, Subject 2, -0.63/-1.27×176 with standard deviations of 0.08/0.09×4 and Subject 3, -0.02/-0.19×29 with standard deviations of 0.14/0.04×45. These values are consistent with expectations within the limits reported by other au-

thors in the agreement between subjective refraction and its estimation from full wavefront aberration data (see for example reference [22]). As the fixation target was the red spot formed on the retina by the probing beam, and the rest of the environment was completely dark, accommodation may have not been fully relaxed, accounting for the myopic shift in Subjects 1 and 2. In addition to this, the larger error in defocus observed in the phase plate and calibration plots discussed before may have had an effect in the measurements. The large standard deviations for the angle in Subjects 1 and 3 are consistent with the very small amount of astigmatism present in those eyes and the larger changes expected in this angle as the two Zernike components change relative to each other in phase with fluctuations of accommodation [23]. As the astigmatism prescription of Subject 2 is much larger, the variability in angle will be much smaller as it will be strongly dependant on the variability of the ratio between C_5 and C_6 in Fig. 6(d) [23]. The behaviour of the higher order aberrations appears to be in line with previous reports of large populations [24–26], although the sample is too small to draw any conclusions in this respect.

6 Conclusion

We have presented a curvature wavefront sensor and demonstrated the feasibility of using it to measure aberrations of the human eye. The layout proposed is novel, and the algorithm proposed has been adapted from previously published work [1,16]. The design of the set-up incorporates two field lenses that, together with a beam separator, define the distance Δz between the two defocused planes. The data obtained was processed using a Gerchberg-type algorithm and the wavefronts reconstructed. The quality of the signal from real eyes enabled the wavefronts to be reconstructed without apparent problems. The characteristics of the reconstructed wavefronts were in line with expectations; that is, defocus and astigmatism behaved as expected from the subjects' prescriptions [22], whilst higher order aberrations seem to behave similarly to previous studies of large populations [24–26], although our sample is too small to draw any conclusions. In summary, we have presented a feasibility study to use the sensor in the eye. We have not characterised the impact that noise in the signal may have in the reconstruction algorithm, nor did we compare this method with other wavefront sensing methods. We are aware of these needs and they will be addressed in

the future.

Acknowledgements

C. Torti was funded by an internal Ph.D. studentship from City University. Additionally this work was partially funded by the National University of Ireland, Galway, sub-contracted to SHARP-EYE FP6 Research Training Network, Contract EC FP-5 HPRN-CT-2002-00301 and by EPSRC, UK Grant GR/S58812/01(P). The authors would like to thank Dr. Salvador X. Bará for providing the phase plate and Brice Thurin from City University for very useful discussions during the undertaking of this work.

References

[1] F. Roddier and C. Roddier. "Wavefront reconstruction using iterative Fourier transforms", Appl. Opt. **30**, 1325 –1327 (1991)

[2] L.N. Thibos, A. Bradley, and X. Hong. "A statistical model of the aberration structure of normal, well corrected eyes", Ophthalmic and Physiological Optics, **22**, 427–433 (2002)

[3] L. Llorente, L. Diaz-Santana, D. Lara-Saucedo, and S. Marcos. "Aberrations of the human eye in visible and near infrared illumination", Optom. Vis. Sci. **80**, 26–35 (2003)

[4] H. Cheng, J.K. Barnett, A.S. Vilupuru, J.D. Marsack, S. Kasthurirangan, R. A. Applegate, and A. Roorda. "A population study on changes in wave aberrations with accommodation", J. of Vision, **4**, 272–280 (2004)

[5] J. Liang, B. Grimm, S. Goelz, and J.F. Bille. "Objective measurement of wave aberration of the human eye with the use of a Hartmann-Shack wave-front sensor", J. Opt. Soc. Am. A., **11**, 1949–1957 (1994)

[6] L. Diaz-Santana, G. Walker, and S. Bará. "Sampling geometries for ocular aberrometry: A model for evaluation of performance", Opt. Express **13**, 8801–8818 (2005)

[7] E. Moreno-Barriuso, S. Marcos, R. Navarro, and S.A. Burns. "Comparing laser ray tracing, spatially resolved refracometer and Hartmann–Shack sensor to measure the ocular wave aberration", Optom. Vis. Sci., **78**, 152–156 (2001)

[8] I. Iglesias, R. Ragazzoni, Y. Julien, and P. Artal. "Extended source pyramid wave-front sensor for the human eye", Opt. Express, **10**, 419–428 (2002)

[9] L. Diaz-Santana, C. Torti, I. Munro, and P. Gasson. "Benefit of higher closed–loop bandwidths in ocular adaptive optics", Opt. Express **11**, 2597–2605 (2003)

[10] F. Diaz-Doutón, J. Pujol, M. Arjona, and S. O. Luque. "Curvature sensor for ocular wavefront measurement", Opt. Lett, **31**, 2245–2247 (2006)

[11] R. Sekine, T. Shibuya, S. Ukai, K.and Komatsu, M. Hattori, T. Mihashi, N. Nakazawa, and Y. Hirohara. "Measurement of wavefront aberration of human eye using Talbot image of two-dimensional grating", Optical Review, **13**, 207–211 (2006)

[12] A. Corbett, T. Wilkinson, J. Zhong, and L. Diaz-Santana. "Designing a holographic modal wave front sensor for the detection of static ocular aberrations", J. Opt. Soc. Am. A., In Press (2007)

[13] S. Gruppetta, L. Koechlin, F. Lacombe, and P. Puget. "A curvature sensor for the measurement of the static corneal topography and the dynamic tear film topography in the human eye", Opt. Lett. **30**, 2757 –2759 (2005)

[14] S. Gruppetta, F. Lacombe, and P. Puget. "Study of the dynamic aberrations of the human tear film", Opt. Express **13**, 7631 –7636 (2005)

[15] Leonard John Otten III, Joshua Lane, Gavin R. G. Erry, Paul Harrison, Lawrence D. Weaver, and G. Martin. "Comparison between a Shack-Hartmann and a distorted grating wavefront sensor", In Anton Kohnle and John D. Gonglewski, editors, Optics in Atmospheric Propagation and Adaptive Systems V, **4884**, 176–185, Agia Pelagia, Crete, Greece, SPIE (2003)

[16] A. Gupta *A wavefront sensor for the human eye based on curvature sensing.* PhD Thesis, Univ. of Arizona (2002).

[17] S. Velghe, J. Primot, N. Guérineau, M. Cohen and B. Wattellier. "Wave-front reconstruction from multidirectional phase derivatives generated by multilateral shearing interferometers", Opt. Lett. **30**, 245–247 (2005)

[18] F. Roddier. "Wavefront sensing and the irradiance transport equation" Appl. Opt. **29**, 1402 –1403 (1990)

[19] M. Soto and E. Acosta and S. Rios. "Performance analysis of curvature sensors: optimum positioning of the measurement planes", Opt. Express **11**, 2577–2588 (2003)

[20] R. Navarro, E. Moreno-Barriuso, S. Bará, and T. Mancebo. "Phase plates for wave-aberration compensation in the human eye", Opt. Lett. **25**, 236–238 (2000)

[21] R.J. Noll. "Zernike polynomials and atmospheric turbulence", J. Opt. Soc. Am., **66**, 207–211 (1976)

[22] X. Cheng and A. Bradley and L.N. Thibos. "Predicting subjective judgment of best focus with objective image quality metrics", J. of Vision **4**, 310–321 (2004)

[23] L. Diaz-Santana, V. Gueriaux, G. Arden, and S. Gruppetta. "New methodology to measure the dynamics of ocular wave front aberrations during small amplitude changes of accommodation". Opt. Express, In Press (2007)

[24] J. Porter, A. Guirao, I. Cox, and D. Williams. "Monochromatic aberrations of the human eye in a large population", J. Opt. Soc. Am. A **18**, 1793–1803 (2001)

[25] J. Castejón-Mochón, N. López-Gil, A. Benito, and P. Artal. "Ocular wave-front aberration statistics in a normal young population", Vis. Res. **42**, 161–1617 (2002)

[26] L. Thibos, X. Hong, A. Bradley, and X. Cheng. "Statistical variation of aberration structure and image quality in a normal population of health eyes", J. Opt. Soc. Am. A **19**, 2329–2348 (2002)

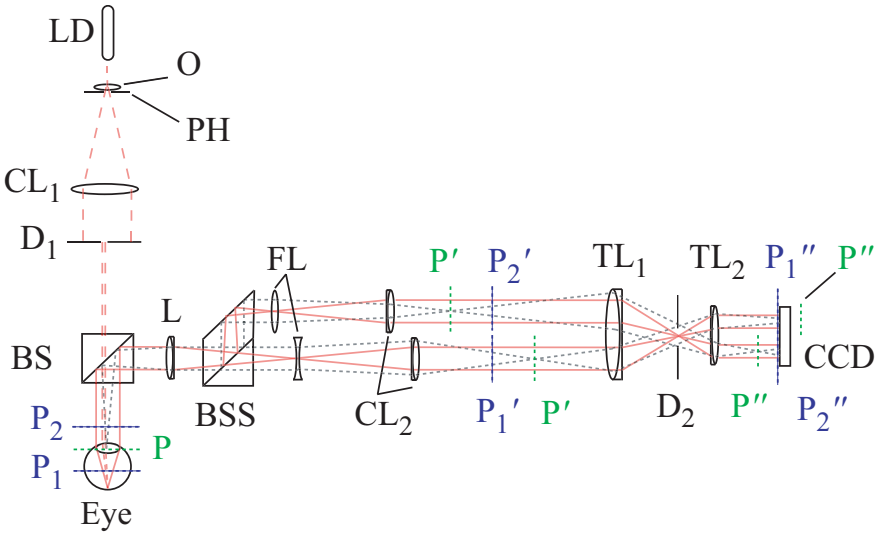

Figure 1. Schematic diagram of the optical system. The incident path of the illuminating light is indicated by dashed red lines while light returning from the eye is indicated by solid red lines. The ray tracing with dashed gray lines help illustrate the locations of pupil conjugates P' and P'' (green). Conjugates of the out-of-focus planes are indicated in blue. The primes denote plane conjugation.

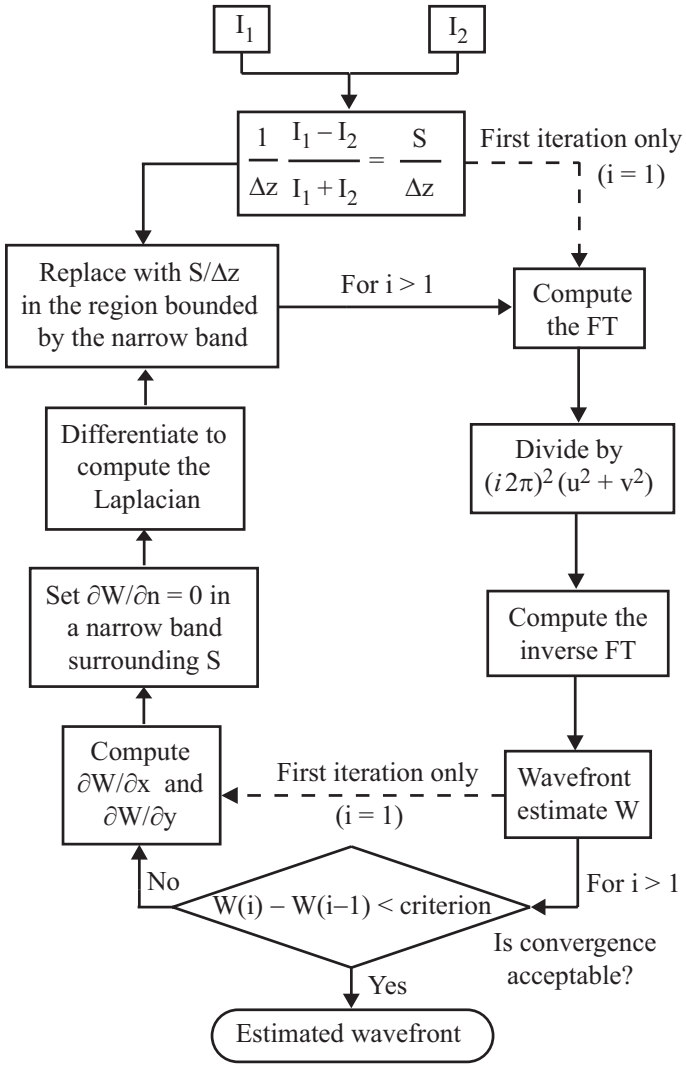

Figure 2. Flow chart of the iterative Gerchberg-type algorithm [1] used for wavefront reconstruction.

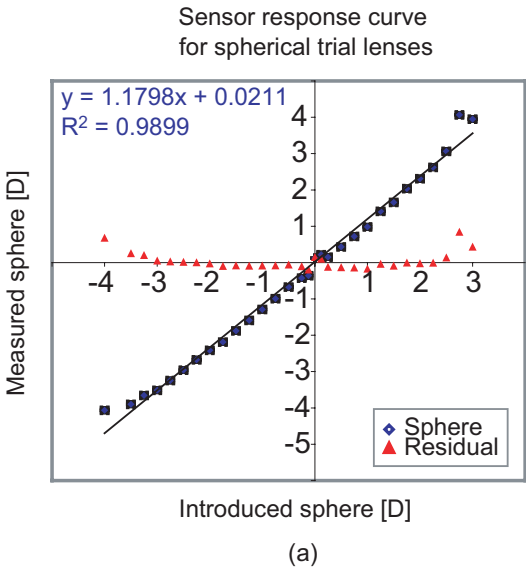

(a)

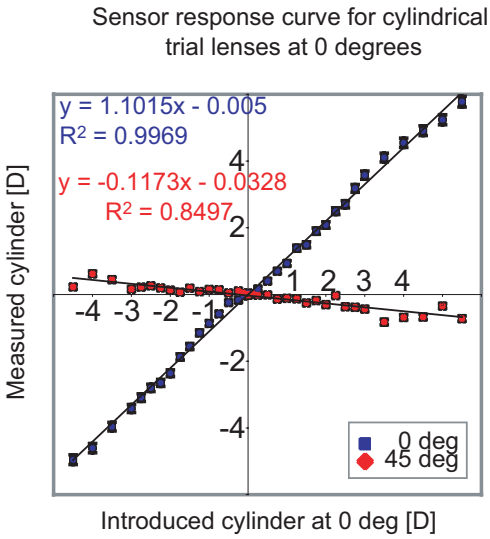

(b)

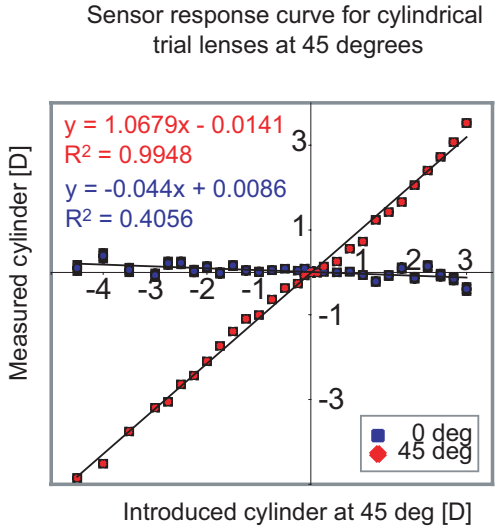

(c)

Figure 3. The sensor response curve for trial lenses. (a) Spherical lenses, (b) Cylindrical lenses oriented at approximately 0° (b) Cylindrical lenses oriented at approximately 45°.

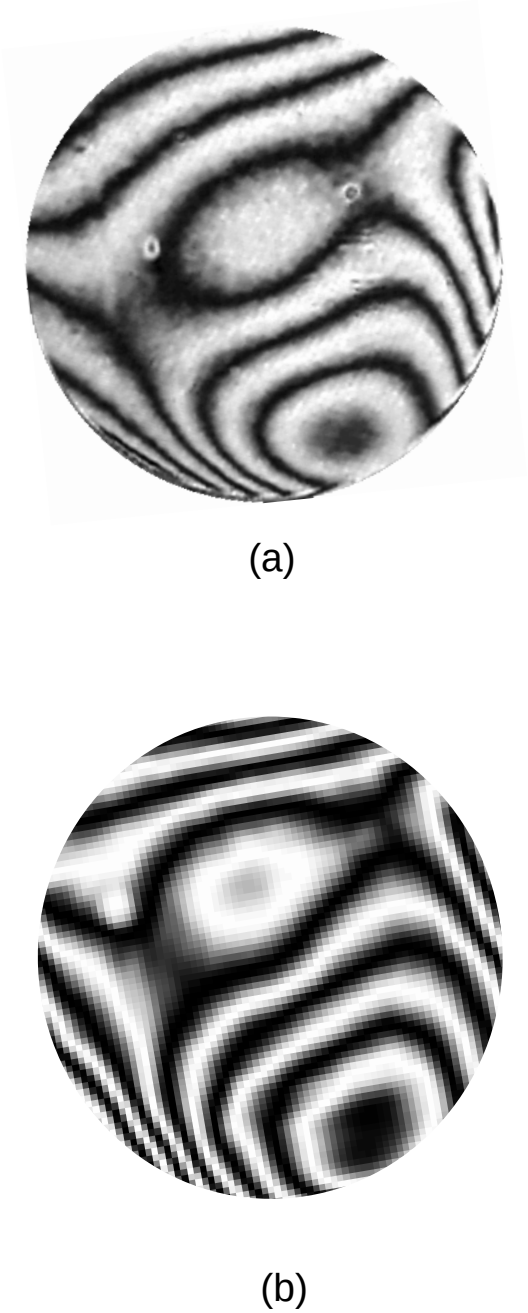

Figure 4. An interferogram of the phase plate obtained from (a) A Mach-Zender interferometer, and (b) The curvature sensor.

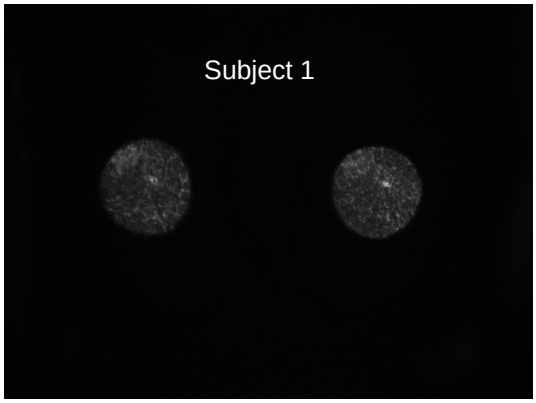

(a)

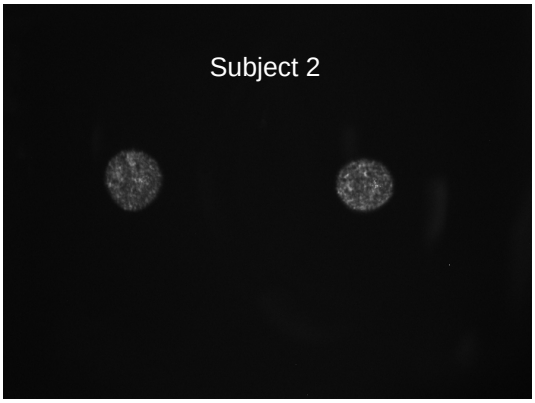

(b)

Figure 5. Defocused pupil images obtained with the CS from real eyes.

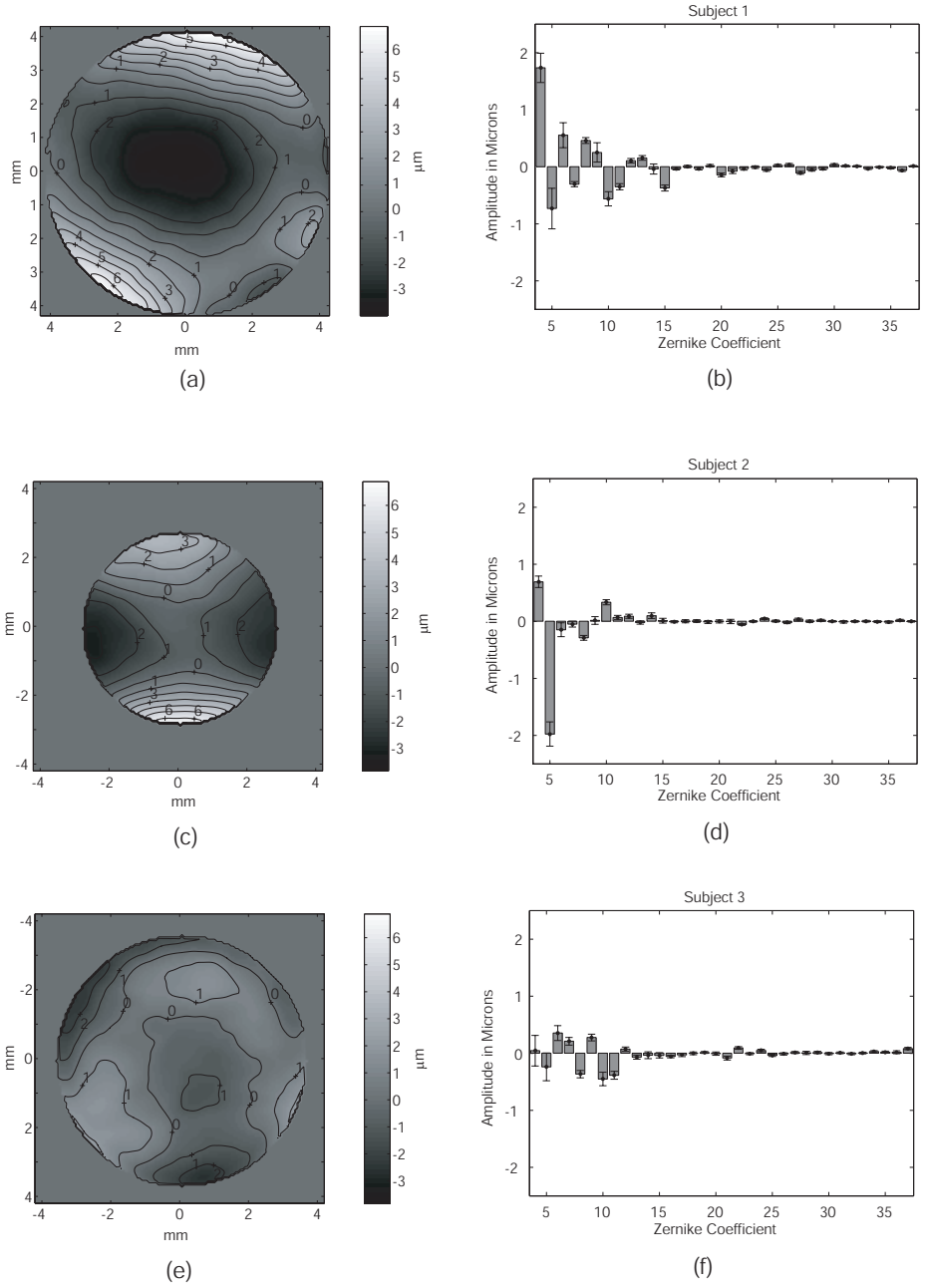

Figure 6. Results obtained from 3 real eyes. The left columns shows the wavefronts retrieved from the curvature sensor data. Right column shows zernike coefficients fitted to the retrieved wavefronts in the same order as used by Noll [21].